

Unconditionally stable method and numerical solution of the hyperbolic phase-field crystal equation

P. K. Galenko*

Friedrich-Schiller-Universität Jena, Physikalisch-Astronomische Fakultät, D-07743 Jena, Germany

H. Gomez

*Department of Mathematical Methods, University of A Coruña,
Campus de Elviña, s/n, 15192 A Coruña, Spain*

N. V. Kropotin

Institut für Materialphysik im Weltraum, Deutsches Zentrum für Luft- und Raumfahrt (DLR), 51170 Köln, Germany

K. R. Elder

Department of Physics, Oakland University, Rochester, MI, 48309-4487, USA

(Dated: July 29, 2013)

The phase-field crystal model (PFC model) resolves systems on atomic length scales and diffusive time scales and lies in between standard phase-field modeling and atomistic methods. More recently a hyperbolic or modified PFC model was introduced to describe fast (propagative) and slow (diffusive) dynamics. We present a finite-element method for solving the hyperbolic PFC-equation, introducing an unconditionally stable time integration algorithm. A spatial discretization is used with the traditional C^0 -continuous Lagrange elements with quadratic shape functions. The space-time discretization of the PFC-equation is second-order accurate in time and is shown analytically to be unconditionally stable. Numerical simulations are used to show a monotonic decrease of the free energy during the transition from the homogeneous state to stripes. Benchmarks on modeling patterns in two dimensional space are carried out. The benchmarks show applicability of the proposed algorithm for determining equilibrium states. Quantitatively, the proposed algorithm is verified for the problem of lattice parameter and velocity selection when a crystal invades a homogeneous unstable liquid.

PACS numbers: 02.70.-c; 05.70.Fh; 05.70.Ln; 64.60.-i

I. INTRODUCTION

The phase-field crystal model (PFC-model) is a continuum model that describes processes on atomic length scales and patterns on the nano- and micro-length scales [1–3]. This model is characterized by a conserved field that is related to the local atomic number density, such that it is spatially periodic in the solid phase and constant in the liquid phase. The model has been related to other continuum field theories such as classical density-functional theory [4, 5] and the atomic density function theory [6]. The PFC-model provides an efficient tool for simulating ordering of nano-scale structures on micron length scales [3], liquid-solid transitions, dislocation motion and plasticity, glass formation and foams, epitaxial growth, grain boundary premelting, crack propagation, surface reconstructions, grain boundary energies, dynamics of colloidal systems and polymers (for an overview, the reader is referred to [7] and the references therein).

Originally formulated in a parabolic form, the PFC model has now been extended to include faster degrees of freedom consistent with inertia due to propagative

regimes of transformation. In particular, a hyperbolic or modified PFC model was introduced which includes an inertial term, and thus allows for the description of both fast and slow dynamics of transformation [8–10]. Fast front dynamics occurs when a system is quenched far below a transition point or far below the equilibrium temperature of the phase transition. These conditions lead to a fast phase transition when the velocity of the front is comparable to the speed of atomic diffusion or the speed of local structural relaxation. The movement of a phase transition front at such fast velocities can lead to the formation of bulk phases that are not in a local structural or chemical equilibrium.

The fascinating physics captured by the hyperbolic PFC-model has triggered a growing interest in the development of computational methods to solve the equation. From a numerical analysis perspective, algorithms for solving the hyperbolic PFC-model have to contend with first and second order time derivatives and six-order spatial derivatives. Therefore, several special numerical methods for solution of the hyperbolic PFC-equation were recently developed. Wise et al. [11] derived a first-order accurate and unconditionally energy stable finite-difference scheme based on a convex splitting of a discrete energy for the parabolic phase-field crystal equation. Similar concepts were applied to the hyperbolic Cahn-

*e-mail: Peter.Galenko@uni-jena.de; Fax: ++49- (3641)-947792

Hilliard and Allen-Cahn equations in Ref. [12]. Subsequently, a second-order accurate finite-difference method was introduced [13, 14], which is unconditionally stable with respect to a discrete version of a quantity entitled as “pseudoenergy”.

In the present paper, we concentrate on the development of a finite-element method for the hyperbolic PFC-equation, introducing a new unconditionally stable time integration algorithm. A space-time discretization of the hyperbolic phase-field crystal equation which is second-order time accurate and unconditionally stable is proposed. Unconditional stability in this context means that the free-energy of the discrete solution decreases (or remains constant) from one step to the next irrespective of the mesh size and the time step. This implies that the algorithm respects the underlying physics of the equation. From a practical point of view, unconditional stability is associated with increased robustness, better behavior of the numerical solution for large time steps, and higher accuracy for long-time calculations. The most common paradigm for achieving unconditional stability in the context of phase transition problems is the so-called Eyre’s method [15, 16], which is widely used in computational physics [17, 18]. Although Eyre’s method was a significant step forward, it has been recently shown that it leads to inaccurate solutions for large time steps [19] because it is only a first-order accurate method. Recently, a generalization of Eyre’s method that achieves unconditional stability has been introduced, but in contrast with Eyre’s method, it is second-order accurate [19, 20]. This generalization has been applied to the phase-field crystal equation [20], using a space discretization that requires the use of globally \mathcal{C}^1 -continuous finite elements [21]. In the present work this algorithm is extended to the hyperbolic (modified) PFC-equation. We introduce a space discretization that can be used with traditional \mathcal{C}^0 -continuous Lagrange finite elements, available in all finite element software packages. As an example, the proposed algorithm is applied to the problem of the lattice parameter and velocity selection when a periodic crystal front invades homogeneous liquid phase.

The paper is organized as follows. The hyperbolic or modified PFC-equation is formulated in Section II. To have a finite element discretization of the modified PFC-equation, a splitting and a variational formulation of the equation are presented in Section III. Spatial and temporal discretization of the equations are shown in Section IV. A numerical approximation of the discrete form is given in Section V using triangular Lagrange elements. In Section VI we present tests for the numerical scheme. Results on the phase diagram and free energy of the entire system are summarized. Section VII is devoted to the numerical solution of the problem of the wave-number and velocity selection of a front invading an unstable phase. Numerical results for the front velocity and wave-number at the front are compared with those obtained previously using marginal stability analysis. Finally, Section VIII

presents a summary of our conclusions.

II. MODIFIED PFC-EQUATION

Let ϕ be a continuous field describing an atomic-scale density. We consider the following free energy functional [12, 22]

$$\mathcal{F}[\phi, \vec{J}] = \mathcal{F}_{eq}[\phi] + \mathcal{F}_{neq}[\vec{J}], \quad (1)$$

with the local equilibrium contribution

$$\mathcal{F}_{eq}[\phi] = \int_{\Omega} \left[F(\phi) - |\vec{\nabla}\phi|^2 + \frac{1}{2}(\nabla^2\phi)^2 \right] d\Omega, \quad (2)$$

and the following pure nonequilibrium contribution

$$\mathcal{F}_{neq}[\vec{J}] = \frac{\tau}{2} \int_{\Omega} \vec{J} \cdot \vec{J} d\Omega, \quad \tau > 0. \quad (3)$$

In Eq. (2) the homogeneous (space independent) part of free energy density is given by

$$F(\phi) = \frac{1-\varepsilon}{2}\phi^2 + \frac{\alpha}{3}\phi^3 + \frac{1}{4}\phi^4, \quad (4)$$

while, in Eq. (3), \vec{J} is a vector field of the flux that satisfies the conservation equation

$$\frac{\partial\phi}{\partial t} + \vec{\nabla} \cdot \vec{J} = 0. \quad (5)$$

where t denotes the time. For the free energy functional defined in Eq. (1) to decrease or remain constant in time, the vector field \vec{J} needs to fulfill the relation

$$\tau \frac{\partial\vec{J}}{\partial t} + \vec{J} = -\vec{\nabla}\mu \quad (6)$$

where the chemical potential μ is given by

$$\mu(\phi) \equiv \frac{\delta\mathcal{F}}{\delta\phi} = \frac{dF(\phi)}{d\phi} + 2\nabla^2\phi + \nabla^4\phi, \quad (7)$$

with

$$\frac{dF(\phi)}{d\phi} = \phi^3 + \alpha\phi^2 + (1-\varepsilon)\phi \equiv f(\phi). \quad (8)$$

In the above expressions, $\varepsilon = (T_c - T)/T_c$ is the governing parameter which characterizes undercooling, T and T_c are the temperature and the critical temperature of transition, respectively, and τ is the relaxation time of the flux \vec{J} to its stationary state. The free-energy density (4) can describe transitions from metastable (as occurs close to first order phase transitions, e.g., in solidification processes) and unstable states (as occurs in second-order phase transitions) to stable ones.

The system of Eqs. (5) and (6) can be re-written in the form

$$\tau \frac{\partial^2\phi}{\partial t^2} + \frac{\partial\phi}{\partial t} = \nabla^2\mu. \quad (9)$$

The hyperbolic equation (9) includes the dissipation described by the traditional parabolic PFC equation [1], as well as an inertial term $\propto \partial^2\phi/\partial t^2$ that accounts for the kinetic contribution (3). Alternatively, Eq. (9) was proposed by Stefanovic et al. [8] to incorporate both fast elastic relaxation and slower mass diffusion.

Introducing the new variable ψ , one can split Eq. (9) as

$$\begin{cases} \frac{\partial\phi}{\partial t} = \psi, \\ \tau \frac{\partial\psi}{\partial t} = \nabla^2\mu - \psi, \end{cases} \quad (10)$$

Using the Helmholtz decomposition theorem, the flux \vec{J} can be unambiguously defined through the expansion of gradient and curl contributions: $\vec{J} = -\vec{\nabla}u + \vec{\nabla} \times \vec{U}$. Now, we notice that the dynamics of the phase variable ϕ is only determined by the divergence of \vec{J} [12], so one can take the divergence of Eq. (6), and use the Helmholtz decomposition of \vec{J} in Eq. (5) to derive the system of partial differential equations

$$\begin{cases} \frac{\partial\phi}{\partial t} = \nabla^2u, \\ \tau \frac{\partial\nabla^2u}{\partial t} = \nabla^2\mu - \nabla^2u, \\ \mu = f(\phi) + 2\nabla^2\phi + \nabla^4\phi. \end{cases} \quad (11)$$

The system of equations (11) is equivalent to the hyperbolic equation (9), and represents a convenient form for developing an unconditionally stable computational schemes [12, 13].

While in principle an equation for the curl of \vec{J} could also be included it is not of much interest since it does not couple to ϕ and decays exponentially in time in such a manner that \mathcal{F}_{neq} always decreases. Thus the contribution of $\vec{\nabla} \times \vec{U}$ to \vec{J} can be ignored.

III. VARIATIONAL FORMULATION

In this section we introduce a variational formulation of the modified phase field crystal equation with the ultimate goal of deriving a finite element discretization. To implement a classical Lagrange finite element scheme it is convenient to introduce the variable θ , such that, $\theta = \nabla^2\phi$, and, following Eqs. (11), we solve the system of equations

$$\begin{cases} \frac{\partial\phi}{\partial t} = \nabla^2u, \\ \tau \frac{\partial\nabla^2u}{\partial t} = \nabla^2\mu - \nabla^2u, \\ \mu = f(\phi) + 2\nabla^2\phi + \nabla^2\theta, \\ \frac{\partial\theta}{\partial t} = \frac{\partial\nabla^2\phi}{\partial t}. \end{cases} \quad (12)$$

The variational problem associated with the system of equations (12) is stated as follows: find ϕ, u, μ, θ such that for all v, w, p, q the following system of equations is satisfied

$$\begin{cases} \int_{\Omega} v \frac{\partial\phi}{\partial t} d\Omega + \int_{\Omega} \vec{\nabla}v \cdot \vec{\nabla}u d\Omega = 0, \\ - \int_{\Omega} \tau \vec{\nabla}w \cdot \frac{\partial\vec{\nabla}u}{\partial t} d\Omega + \int_{\Omega} \vec{\nabla}w \cdot \vec{\nabla}\mu d\Omega - \int_{\Omega} \vec{\nabla}w \cdot \vec{\nabla}u d\Omega = 0, \\ \int_{\Omega} p[\mu - f(\phi)] d\Omega + \int_{\Omega} 2\vec{\nabla}p \cdot \vec{\nabla}\phi d\Omega + \int_{\Omega} \vec{\nabla}p \cdot \vec{\nabla}\theta d\Omega = 0, \\ \int_{\Omega} q \frac{\partial\theta}{\partial t} d\Omega + \int_{\Omega} \vec{\nabla}q \cdot \frac{\partial\vec{\nabla}\phi}{\partial t} d\Omega = 0, \end{cases} \quad (13)$$

which assumes free-flux conditions for all variables on the surface Γ for the volume Ω . Due to their integral form, equations (13) present a weak form of differential

equations (12).

We show now that equations (13), which are equivalent to the modified phase-field crystal equation (9), lead to a

stable evolution of the system such that the free energy of the entire system does not increase in time, i.e.,

$$\frac{d\mathcal{F}(\phi, \vec{J})}{dt} = \int_{\Omega} \left(\frac{\delta\mathcal{F}}{\delta\phi} \frac{\partial\phi}{\partial t} + \frac{\delta\mathcal{F}}{\delta\vec{J}} \cdot \frac{\partial\vec{J}}{\partial t} \right) d\Omega \leq 0. \quad (14)$$

Using the balance (5), one can obtain from Eqs. (1) and (3) that the free energy (14) is given by

$$\begin{aligned} \frac{d\mathcal{F}(\phi, \vec{J})}{dt} &= - \int_{\Omega} \mu \vec{\nabla} \cdot \vec{J} d\Omega + \int_{\Omega} \tau \vec{J} \cdot \frac{\partial\vec{J}}{\partial t} d\Omega \\ &= \int_{\Omega} \mu \frac{\partial\phi}{\partial t} d\Omega + \int_{\Omega} \tau \vec{J} \cdot \frac{\partial\vec{J}}{\partial t} d\Omega \end{aligned} \quad (15)$$

with $\vec{J} = 0$ on Γ . Taking $v = \mu$, and $w = u$ in Eq. (13) and combining the first two equations, one gets

$$\int_{\Omega} \mu \frac{\partial\phi}{\partial t} d\Omega + \int_{\Omega} \tau \vec{\nabla} u \cdot \frac{\partial\vec{\nabla} u}{\partial t} d\Omega + \int_{\Omega} \vec{\nabla} u \cdot \vec{\nabla} u d\Omega = 0. \quad (16)$$

The first equation in Eqs. (11) and the balance (5) lead to $\vec{\nabla} \cdot (\vec{J} + \vec{\nabla} u) = 0$. Using again the Helmholtz decomposition of \vec{J} , we note that the last equation is unaffected by the term $\vec{\nabla} \times \vec{U}$, so we may just take

$$\vec{J} = -\vec{\nabla} u. \quad (17)$$

Substituting the latter relation between \vec{J} and u into Eq. (15) gives

$$\frac{d\mathcal{F}(\phi, \vec{J})}{dt} = \int_{\Omega} \mu \frac{\partial\phi}{\partial t} d\Omega + \int_{\Omega} \tau \vec{\nabla} u \cdot \vec{\nabla} \frac{\partial u}{\partial t} d\Omega. \quad (18)$$

Comparing Eq. (18) with equation (16) we obtain the stability condition

$$\frac{d\mathcal{F}(\phi, \vec{J})}{dt} = - \int_{\Omega} \vec{\nabla} u \cdot \vec{\nabla} u d\Omega \leq 0, \quad (19)$$

which confirms Eq. (14) for stable evolution of the entire system.

In consideration of the variational formulation (13) we have now shown an important feature of the free energy \mathcal{F} which has classical contribution consistent with the local equilibrium processes and the additional kinetic contribution for description of fast transitions on the scale of τ , Eq. (1). Namely, the sign of the free energy time derivative in Eqs. (14) and (19) shows that \mathcal{F} can be considered as a Lyapunov function — a function that is non-increasing in time and determines the stability of the system.

IV. STABLE NUMERICAL SCHEME

A. Discretization

We now discretize the variational form (13) replacing the relevant functions with their discrete counterparts that will be denote with an h superscript. Then, it follows that

$$\left\{ \begin{aligned} \int_{\Omega} v^h \frac{\partial\phi^h}{\partial t} d\Omega + \int_{\Omega} \vec{\nabla} v^h \cdot \vec{\nabla} u^h d\Omega &= 0, \\ - \int_{\Omega} \tau \vec{\nabla} w^h \cdot \frac{\partial\vec{\nabla} u^h}{\partial t} d\Omega + \int_{\Omega} \vec{\nabla} w^h \cdot \vec{\nabla} \mu^h d\Omega - \int_{\Omega} \vec{\nabla} w^h \cdot \vec{\nabla} u^h d\Omega &= 0, \\ \int_{\Omega} p^h [\mu^h - f(\phi^h)] d\Omega + \int_{\Omega} 2\vec{\nabla} p^h \cdot \vec{\nabla} \phi^h d\Omega + \int_{\Omega} \vec{\nabla} p^h \cdot \vec{\nabla} \theta^h d\Omega &= 0, \\ \int_{\Omega} q^h \frac{\partial\theta^h}{\partial t} d\Omega + \int_{\Omega} \vec{\nabla} q^h \cdot \frac{\partial\vec{\nabla} \phi^h}{\partial t} d\Omega &= 0. \end{aligned} \right. \quad (20)$$

The system of equations (20) is a semi-discretized numerical scheme, i.e., it represents the spatial discretization of Eqs. (13).

To obtain the time discretization algorithm, the time interval of interest $[0, T]$ is subdivided into N uniform subintervals $\mathcal{I}_n = (t_n, t_{n+1})$ where $t_{n+1} - t_n = \Delta t$; $n =$

$0, \dots, N-1$. The discrete approximation of $\phi^h(t_n)$ is notated as ϕ_n^h , where the dependence on the spatial coordinate is omitted for simplicity. Analogous notation is used for other functions of interest. Special notations $\{\{\phi_n^h\}\} = \phi_{n+1}^h - \phi_n^h$ and $\phi_{n+1/2}^h = \frac{1}{2}(\phi_{n+1}^h + \phi_n^h)$ are also used below. We propose an algorithm which may be thought of as a second-order accurate generalization of Eyre's method [15]. However, rather than splitting the free energy into a concave and convex parts as in Eyre's method, we split it as follows:

$$F(\phi) = F_+(\phi) + F_-(\phi), \quad (21)$$

where $F_+^{(iv)}(\phi) \geq 0$, $F_-^{(iv)}(\phi) \leq 0$, and the superscript (iv) denotes the fourth derivative. The advantage of this splitting over Eyre's splitting is that it permits de-

termining a second-order accurate and unconditionally stable method in contrast with Eyre's method which is only first order accurate. As shown for the dynamics of phase separation [19], the use of a second-order accurate method permits taking time steps several orders of magnitude larger than those required by the first-order accurate method. We also note that although for the modified phase field crystal equation, in which one gets $F_- = 0$, we will present the method in its full generality, assuming that both F_+ and F_- are non-zero. The general method would be useful, for example, for phase-field crystal equations, based on logarithmic potentials (which give $F_- \neq 0$). We will also use the notation $f_+(\phi) = F_+'(\phi)$ and $f_-(\phi) = F_-'(\phi)$. Then, our algorithm, Eqs. (20), may be written as follows:

$$\left\{ \begin{array}{l} \int_{\Omega} v^h \frac{\{\{\phi_n^h\}\}}{\Delta t} d\Omega + \int_{\Omega} \vec{\nabla} v^h \cdot \vec{\nabla} u_{n+1/2}^h d\Omega = 0, \\ - \int_{\Omega} \tau \vec{\nabla} w^h \cdot \frac{\{\{\vec{\nabla} u_n^h\}\}}{\Delta t} d\Omega + \int_{\Omega} \vec{\nabla} w^h \cdot \vec{\nabla} \mu_{n+1/2}^h d\Omega - \int_{\Omega} \vec{\nabla} w^h \cdot \vec{\nabla} u_{n+1/2}^h d\Omega = 0, \\ \int_{\Omega} p^h \mu_{n+1/2}^h d\Omega - \int_{\Omega} p^h \frac{1}{2} [f(\phi_{n+1}^h) + f(\phi_n^h)] d\Omega + \int_{\Omega} p^h \frac{\{\{\phi_n^h\}\}^2}{12} (f_+'(\phi_n^h) + f_-'(\phi_{n+1}^h)) d\Omega \\ + \int_{\Omega} 2\vec{\nabla} p^h \cdot \vec{\nabla} \phi_{n+1/2}^h d\Omega + \int_{\Omega} \vec{\nabla} p^h \cdot \vec{\nabla} \theta_{n+1/2}^h d\Omega = 0, \\ \int_{\Omega} q^h \frac{\{\{\theta_n^h\}\}}{\Delta t} d\Omega + \int_{\Omega} \vec{\nabla} q^h \cdot \vec{\nabla} \left(\frac{\{\{\phi_n^h\}\}}{\Delta t} \right) d\Omega = 0. \end{array} \right. \quad (22)$$

The system of equations (22) is a fully-discretized numerical scheme, i.e., it represents the temporal and spatial discretization of Eqs. (13). As we will see in the next section, the appearance of the second and third terms in the third equation lead to an unconditionally stable discretization of the nonlinear term.

B. Stability

To show that the algorithm inherits the stability condition of the continuous theory, $d\mathcal{F}/dt < 0$ [see Eqs. (14) and (19)], we need to take into account the following quadrature formulas: Let $g : [a, b] \mapsto \mathbb{R}$ be a sufficiently

smooth function. The following relations hold [19]:

$$\int_a^b g(x) dx = \frac{b-a}{2} [g(a) + g(b)] - \frac{(b-a)^3}{12} g''(a) - \frac{(b-a)^4}{24} g'''(\chi_+); \quad \chi_+ \in (a, b), \quad (23)$$

$$\int_a^b g(x) dx = \frac{b-a}{2} [g(a) + g(b)] - \frac{(b-a)^3}{12} g''(b) + \frac{(b-a)^4}{24} g'''(\chi_-); \quad \chi_- \in (a, b). \quad (24)$$

Let us consider the trivial identity

$$\int_{\phi_n^h}^{\phi_{n+1}^h} F_+'(z) dz = \int_{\phi_n^h}^{\phi_{n+1}^h} f_+(z) dz, \quad (25)$$

If we integrate directly the left hand side of the equation, and apply the quadrature formula (23) to the right hand side, we obtain

$$\begin{aligned} \{\{F_+(\phi_n^h)\}\} &= \frac{\{\{\phi_n^h\}\}}{2} [f_+(\phi_n^h) + f_+(\phi_{n+1}^h)] \\ &- \frac{\{\{\phi_n^h\}\}^3}{12} f_+''(\phi_n^h) \\ &- \frac{\{\{\phi_n^h\}\}^2}{24} f_+'''(\phi_{n+\xi_+}^h), \quad \xi_+ \in (0, 1). \end{aligned} \quad (26)$$

$$\begin{aligned} &\frac{\{\{F_-(\phi_n^h)\}\}}{\{\{\phi_n^h\}\}} - \frac{\{\{\phi_n^h\}\}^3}{24} f_-'''(\phi_{n+\xi_-}^h) \\ &= \frac{1}{2} [f_-(\phi_n^h) + f_-(\phi_{n+1}^h)] \\ &- \frac{\{\{\phi_n^h\}\}^2}{12} f_-''(\phi_{n+1}^h); \quad \xi_- \in (0, 1). \end{aligned} \quad (29)$$

Rearranging Eq. (26), it follows that

$$\begin{aligned} &\frac{\{\{F_+(\phi_n^h)\}\}}{\{\{\phi_n^h\}\}} + \frac{\{\{\phi_n^h\}\}^3}{24} f_+'''(\phi_{n+\xi_+}^h) \\ &= \frac{1}{2} [f_+(\phi_n^h) + f_+(\phi_{n+1}^h)] \\ &- \frac{\{\{\phi_n^h\}\}^2}{12} f_+''(\phi_n^h), \quad \xi_+ \in (0, 1). \end{aligned} \quad (27)$$

Analogously, applying quadrature (24) to the identity

$$\int_{\phi_n^h}^{\phi_{n+1}^h} F'_-(z) dz = \int_{\phi_n^h}^{\phi_{n+1}^h} f_-(z) dz, \quad (28)$$

and operating, one obtains

We now show that with the choices

$$\begin{aligned} v^h &= \mu_{n+1/2}^h, \quad w^h = u_{n+1/2}^h, \quad p^h \\ &= \frac{\{\{\phi_n^h\}\}}{\Delta t}, \quad q^h = \theta_{n+1/2}^h, \end{aligned} \quad (30)$$

the stability condition is inherited by the discrete formulation for arbitrary time step size. Indeed, from (22) one gets

$$\left\{ \begin{aligned} &\int_{\Omega} \mu_{n+1/2}^h \frac{\{\{\phi_n^h\}\}}{\Delta t} d\Omega + \int_{\Omega} \vec{\nabla} \mu_{n+1/2}^h \cdot \vec{\nabla} u_{n+1/2}^h d\Omega = 0, \\ &-\int_{\Omega} \tau \vec{\nabla} u_{n+1/2}^h \cdot \frac{\{\{\vec{\nabla} u_n^h\}\}}{\Delta t} d\Omega + \int_{\Omega} \vec{\nabla} u_{n+1/2}^h \cdot \vec{\nabla} \mu_{n+1/2}^h d\Omega - \int_{\Omega} \vec{\nabla} u_{n+1/2}^h \cdot \vec{\nabla} u_{n+1/2}^h d\Omega = 0, \\ &\int_{\Omega} \frac{\{\{\phi_n^h\}\}}{\Delta t} \mu_{n+1/2}^h d\Omega - \int_{\Omega} \frac{\{\{\phi_n^h\}\}}{\Delta t} \frac{1}{2} [f(\phi_{n+1}^h) + f(\phi_n^h)] d\Omega + \int_{\Omega} \frac{\{\{\phi_n^h\}\}^3}{12\Delta t} (f_+''(\phi_n^h) + f_-''(\phi_{n+1}^h)) d\Omega \\ &+ \int_{\Omega} 2\vec{\nabla} \left(\frac{\{\{\phi_n^h\}\}}{\Delta t} \right) \cdot \vec{\nabla} \phi_{n+1/2}^h d\Omega + \int_{\Omega} \vec{\nabla} \left(\frac{\{\{\phi_n^h\}\}}{\Delta t} \right) \cdot \vec{\nabla} \phi_{n+1/2}^h d\Omega = 0, \\ &\int_{\Omega} \theta_{n+1/2}^h \frac{\{\{\theta_n^h\}\}}{\Delta t} d\Omega + \int_{\Omega} \vec{\nabla} \theta_{n+1/2}^h \cdot \vec{\nabla} \left(\frac{\{\{\phi_n^h\}\}}{\Delta t} \right) d\Omega = 0. \end{aligned} \right. \quad (31)$$

Rearranging Eqs. (31) and using the identities (27) and (29), it follows that

$$\begin{aligned} \frac{1}{\Delta t} \{\{\mathcal{F}\}\} &= - \int_{\Omega} \vec{\nabla} u_{n+1/2}^h \cdot \vec{\nabla} u_{n+1/2}^h d\Omega \\ &- \int_{\Omega} \frac{\{\{\phi_n^h\}\}^4}{24\Delta t} [f_+'''(\phi_{n+\xi_+}^h) - f_-'''(\phi_{n+\xi_-}^h)] d\Omega. \end{aligned} \quad (32)$$

Since f_+''' is a positive function and f_-''' is negative, the

stability condition (19) is proven.

In equation (32), the first term corresponds to the physical dissipation, while the second term corresponds to numerical dissipation. The second term tends to zero as we reduce the time step.

Thus, our algorithm, which follows directly from the system of equations (22), is second-order time accurate. This is a consequence of the linear terms being approx-

imated with a midpoint-type method and the nonlinear terms being handled with a higher-order generalization of the trapezoidal rule.

V. NUMERICAL APPROXIMATION AND SOLUTION

Before choosing the finite element spaces, a few remarks about non-linearity of the equations are in order. To reduce the nonlinearity of the system (22) it is useful to linearize the cubic and quadratic terms (ϕ_{n+1}^3 and ϕ_{n+1}^2) in the function $f(\phi)$ in the following form:

$$(\phi_{n+1}^h)^3 \approx 3(\phi_n^h)^2 \phi_{n+1}^h - 2(\phi_n^h)^3, \quad (33)$$

$$(\phi_{n+1}^h)^2 \approx 2\phi_n^h \phi_{n+1}^h - (\phi_n^h)^2. \quad (34)$$

Linearizing quadratic terms (34) further reduces the order of terms in equations and decrease their nonlinearity (similarly to the previous analyses [23] where the cubic contributions of the kind of $(\phi_{n+1}^h)^3$ were linearized). We note that by linearizing the cubic term, the unconditional stability of the algorithm is lost on a theoretical level. We performed a number of simulations with the linearized algorithm and always found non-increasing energy in the numerical solutions. Thus, we believe our linearly im-

PLICIT scheme is a good compromise between stability and efficiency.

After the above remarks on linearization, an approximation for the functions ϕ^h , u^h , μ^h , and θ^h should be done by choosing the finite element spaces in Eqs. (22). We search the solution using triangular Lagrange elements with quadratic shape functions. Every function can be approximated as a sum of basic functions multiplied by solutions in grid nodes [24]:

$$\begin{aligned} \phi_{n+1}^h &= \sum_i \Phi_{n+1}^i \eta_{n+1}^i, & u_{n+1}^h &= \sum_i U_{n+1}^i \eta_{n+1}^i, \\ \mu_{n+1}^h &= \sum_i \Psi_{n+1}^i \eta_{n+1}^i, & \theta_{n+1}^h &= \sum_i \Theta_{n+1}^i \eta_{n+1}^i \end{aligned} \quad (35)$$

where η_{n+1}^i are the shape functions used for the discretization of the $n+1$ time step, and Φ_{n+1}^i , U_{n+1}^i , Ψ_{n+1}^i , Θ_{n+1}^i are the unknown nodal values of the solution for the functions ϕ_{n+1}^h , u_{n+1}^h , μ_{n+1}^h and θ_{n+1}^h , respectively. Choosing the same mesh on each time step, we have equal shape functions $\eta_{n+1}^i = \eta_n^i = \eta^i$. In the case of adaptive mesh, the shape functions are not equal, so one would compute integrals containing the shape functions defined on two meshes as it is shown below. Thus, substituting approximations (35) into equations (22) gives

$$\begin{pmatrix} M_{n+1} & \frac{\Delta t}{2} A_{n+1} & 0 & 0 \\ 0 & \frac{2\tau + \Delta t}{\Delta t} A_{n+1} & -A_{n+1} & 0 \\ -P_{n+1} + 2A_{n+1} & 0 & M_{n+1} & A_{n+1} \\ A_{n+1} & 0 & 0 & M_{n+1} \end{pmatrix} \begin{pmatrix} \Phi_{n+1} \\ U_{n+1} \\ \Psi_{n+1} \\ \Theta_{n+1} \end{pmatrix} = \begin{pmatrix} M_{n+1,n} \Phi_n - \frac{\Delta t}{2} A_{n+1,n} U_n \\ \frac{2\tau - \Delta t}{\Delta t} A_{n+1,n} U_n + A_{n+1,n} \Psi_n \\ -M_{n+1,n} \Psi_n + P^e - 2A_{n+1,n} \Phi_n - A_{n+1,n} \Theta_n \\ A_{n+1,n} \Phi_n + M_{n+1,n} \Theta_n \end{pmatrix}, \quad (36)$$

where

$$\begin{aligned} M_{n+1} &= (\eta_{n+1}^i, \eta_{n+1}^j), & A_{n+1} &= (\vec{\nabla} \eta_{n+1}^i, \vec{\nabla} \eta_{n+1}^j), \\ P_{n+1} &= (\{2\alpha \phi_n + 3\phi_n^2 + [1 - \varepsilon]\} \eta_{n+1}^i, \eta_{n+1}^j), \\ M_{n+1,n} &= (\eta_{n+1}^i, \eta_n^j), & A_{n+1,n} &= (\vec{\nabla} \eta_{n+1}^i, \vec{\nabla} \eta_n^j), \\ P^e &= (\{[1 - \varepsilon] \phi_n - \phi_n^3\}, \eta_{n+1}^i), \end{aligned} \quad (37)$$

and (\cdot, \cdot) is usual scalar product. As a result, Eqs. (36) together with Eq. (35) and (37) represent Eqs. (22) in the operator form.

VI. BENCHMARKS

In this work only results of modeling for transformation from unstable state are presented with $\alpha = 0$ in

Eq. (4) and (37). Since the system of equations Eqs. (36) is nonsymmetric it was solved by a GMRES-solver in the finite element toolbox FreeFEM++ [25]. We use adapted mesh to the Hessian with the method and algorithm for the mesh generation from Ref. [26].

A. Phase Diagram

The computational scheme was used to examine the evolution from a random non-equilibrium state to verify that the scheme does lead to the expected states. This evolution is made in comparison with the phase diagram in the coordinates “undercooling ε – averaged atomic density field $\langle \phi \rangle$ ” (see, for details, Ref. [2]). In two spatial dimensions, for small values of ε , the phase diagram contains three equilibrium states, a constant homogeneous state, stripes and a triangular distribution of drops. Re-

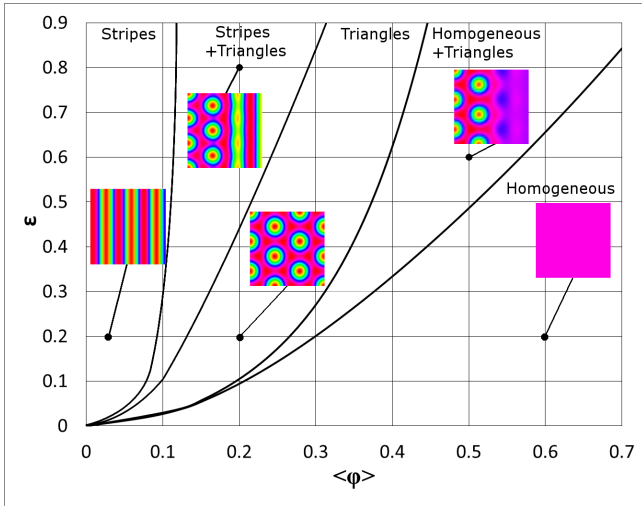


FIG. 1: (color on the web) Phase diagram of two-dimensional patterns as predicted by the solution of Eqs. (38)-(43). Solid points indicate initial values for the undercooled homogeneous phase $\langle\phi\rangle$. Pictures in different regions of phase diagram show the finally evolved patterns modeled by Eqs. (36).

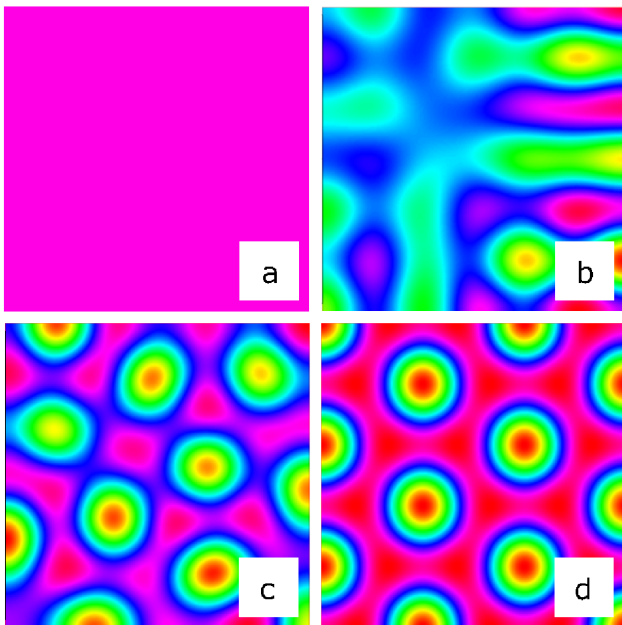


FIG. 2: (color on the web) Evolution of the undercooled homogeneous state to stable equilibrium triangle pattern: (a) $t = 0$; (b) $t = 5 \cdot 10^4$; (c) $t = 10^5$; (d) $t = 2 \cdot 10^5$. Averaged field $\langle\phi\rangle = 0.2$ has been initially undercooled by $\epsilon = 0.2$.

regions of phase coexistence are determined by the Maxwell equal-area construction rule [2]: coexisting phases must have equal chemical potentials under constant pressures of the coexisting phases. Sets of equations for two spatial dimensions with “homogeneous state–triangles” and

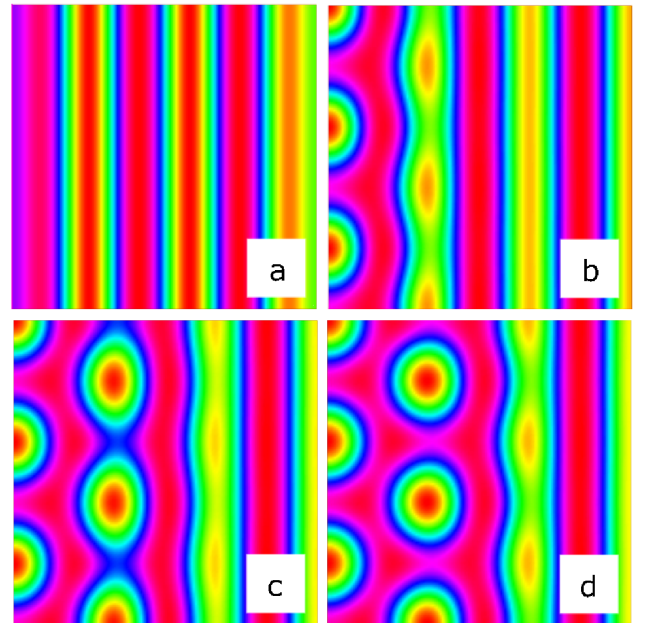


FIG. 3: (color on the web) Transformation of undercooled stripes to equilibrium coexistence of stripes and triangles: (a) $t = 0$; (b) $t = 5 \cdot 10^4$; (c) $t = 10^5$; (d) $t = 2 \cdot 10^5$. Averaged field $\langle\phi\rangle = 0.2$ has been initially undercooled by $\epsilon = 0.8$.

“stripes–triangles” are described as

$$\begin{cases} \mu(\phi_t) = \mu(\phi_h), \\ F_t - F_h = \mu(\phi_h)(\phi_t - \phi_h), \end{cases} \quad (38)$$

$$\begin{cases} \mu(\phi_t) = \mu(\phi_s), \\ F_t - F_s = \mu(\phi_s)(\phi_t - \phi_s), \end{cases} \quad (39)$$

where F , ϕ , μ are the free energy density, coexistence density of phases and chemical potentials, respectively. Subscripts t , s , h denote corresponding phases: triangles, stripes, homogeneous, respectively. For small ϵ these phases can be described by

$$\begin{aligned} \phi_h &= \langle\phi\rangle, & \phi_s &= A_s \sin(q_s x) + \langle\phi\rangle, \\ \phi_t &= A_t \cos(q_t x) \cos(q_t y / \sqrt{3}) \\ &\quad - A_t \cos(2q_t y / \sqrt{3}) / 2 + \langle\phi\rangle, \end{aligned} \quad (40)$$

where the quantities q and A give minimum of the free energy as:

$$\begin{aligned} q_s &= 1, & A_s &= 2\sqrt{\epsilon/3 - \langle\phi\rangle^2}, & q_t &= \sqrt{3}/2, \\ A_t &= \frac{4}{5} \left(\langle\phi\rangle + \frac{1}{3} \sqrt{15\epsilon - 36\langle\phi\rangle^2} \right). \end{aligned} \quad (41)$$

Free energy densities of phases in the one-mode approximation are given by [2]

$$F_h = (1 - \epsilon) \frac{\langle\phi\rangle^2}{2} + \frac{\langle\phi\rangle^4}{4},$$

$$F_s = -\frac{\varepsilon^2}{6} + \frac{(1+\varepsilon)\langle\phi\rangle^2}{2} - 5\frac{\langle\phi\rangle^4}{4}, \quad (42)$$

$$F_t = -0.1\left(\varepsilon^2 + \frac{13}{50}\langle\phi\rangle^4\right) + \frac{\langle\phi\rangle^2}{2} + \frac{4\phi}{25}\sqrt{15\varepsilon - 36\langle\phi\rangle^2}\left(\frac{4}{5}\langle\phi\rangle^2 - \frac{\varepsilon}{3}\right). \quad (43)$$

Figure 1 shows regions of the phase existence and coexistence which are divided by the boundaries obtained from the solution of Eqs. (38)-(43). Numerical simulations were conducted at various values of $\langle\phi\rangle$ and ε with an initial condition containing small random fluctuations in ϕ about $\langle\phi\rangle$. The results of the simulated patterns are shown in Fig. 1 and in each case are consistent with analytic one-mode calculations.

Sample time evolutions of the system from a homogeneous to a triangular state are shown in Fig. 2 and from a stripe state to a stripe/triangular coexistence is depicted in Fig. 3. The following parameters were used in these simulations, $(\tau, \langle\phi\rangle, \Delta t, \Delta x) = (0.1, 0.2, 0.01, 0.1)$ in a system of size 190×190 grid points. The undercooling ε was 0.2 and 0.8 for Fig. 2 and 3, respectively. Both results are consistent with the calculated phase diagram shown in Fig. 1.

We also note that the boundaries in the phase diagram of Fig. 1 have been calculated using one-mode approximation which is the first approximation to solution of the PFC-equation (9) only at small undercooling ε and $\tau \rightarrow 0$. Consequently the numerical solutions will deviate from the analytic calculations for larger undercoolings.

B. Unconditional stability

The algorithm and discrete scheme deliver unconditional stability of numerical computations. The time step Δt can be arbitrary chosen and it is limited only by the requirement of computational accuracy. The stability of the presented algorithm has been verified numerically in a series of computations with different values for space and time discretization.

To demonstrate unconditional stability, evolution of the free energy is analyzed. The free energy (1)-(4) has been taken in the following form

$$\mathcal{F}(\phi, \vec{J}) = \int_{\Omega} \left[F(\phi) - |\vec{\nabla}\phi|^2 + \frac{1}{2}(\nabla^2\phi)^2 + \frac{\tau}{2}|\vec{\nabla}u|^2 \right] d\Omega. \quad (44)$$

The energy (44) is defined by a local equilibrium part described by the slow variable ϕ and a local nonequilibrium part, $\propto J^2 = |\vec{\nabla}u|^2$, corresponding to the kinetic contribution of the free energy [27] in terms of the fast variable \vec{J} . Thus, we shall plot the evolution of the energy (1)-(4).

Figure 4 shows the evolution of the free energy functional \mathcal{F} described by Eq. (44) for different values of the relaxation time τ . As it can be seen, \mathcal{F} monotonically

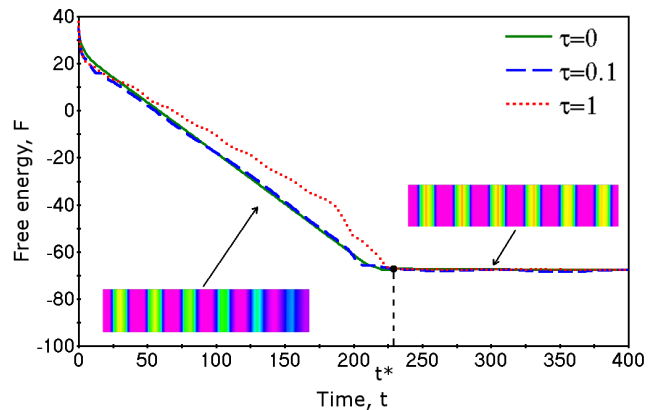


FIG. 4: (color on the web) Transition from initially homogeneous state to stripes. The homogeneous state has been quenched at $\varepsilon = 0.2$ and $\langle\phi\rangle = 0.02$. Numeric parameters were chosen as $(\Delta t, \Delta x) = (0.005, 0.1)$. The free energy functional \mathcal{F} from Eq. (44) decreases monotonically with time for the developing stripes during the computational time $0 < t < t^*$ (see the developing pattern in the left part). The free energy functional \mathcal{F} has a constant values in modeling with $t > t^*$ (see the steady pattern in the right part).

decreases during the computational time $0 < t < t^*$ for the transition from the initially undercooled homogeneous state to stripes. With $t > t^*$, the steadily stable stripes exhibit a constant value of \mathcal{F} for all values of τ tested in this work. The behavior of \mathcal{F} shown in Fig. 4 is similar to that obtained for the crystal growth in a supercooled liquid described by the parabolic PFC-equation (see Fig. 2 in Ref. [20]). This clearly supports our theoretical results obtained for the algorithm, computational scheme, and approximation of functions.

VII. VELOCITY AND WAVE-NUMBER AT THE FRONT INVADING UNSTABLE PHASE

Patterns that emerge when the interface or front invades an excitable or unstable media, has been of interest in many physical phenomena [28]. In this section the numerical method developed in this work will be used to find the velocity and wavelength of a periodic pattern that emerges as a phase-front sweeps through an unstable phase. The results can be quantitatively compared with the predictions of the marginal stability analysis on the wavelength selection at the front of periodic pattern described by the hyperbolic PFC equation [22]. The predictions for front velocities and wavelength selection from marginal stability have been numerically verified in other pattern forming models, such as a phase field model of a superheated solid invading an undercooled melt at large undercoolings [29].

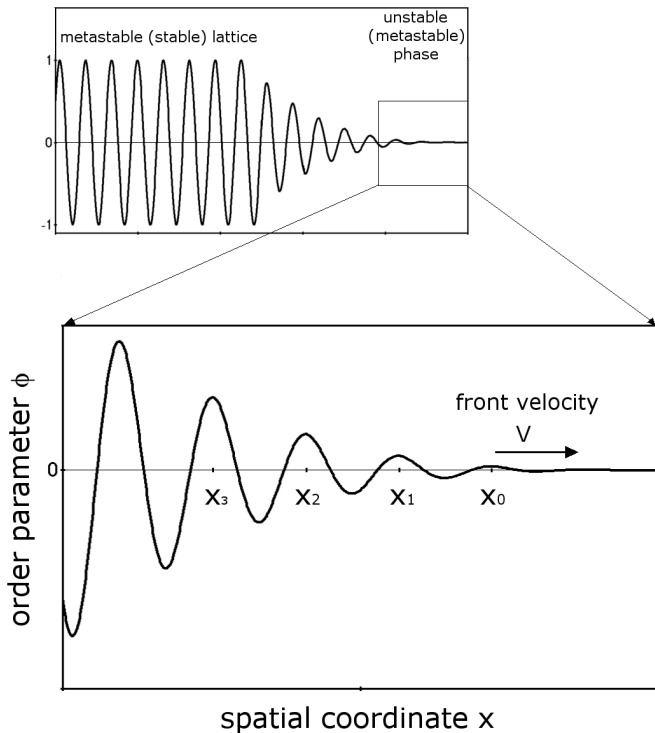


FIG. 5: Front of periodic pattern described by PFC-model. The selected lattice parameter (or wavelength) on the front invading un(meta)stable phase should be measured at the farthest away point significant growth of amplitude of periodic pattern as is shown in inset. x_0 is the point from which the lattice parameter (wavelength) begins to be calculated.

A. Marginal stability analysis

Let us consider a front between a periodic striped pattern and a spatially homogeneous unstable state at $\langle \phi \rangle \rightarrow 0$, such the periodic state is the lowest energy state for all undercoolings, ϵ (see phase diagram plotted in Fig. 1). The situation is depicted in Fig. 5. The goal of this work is to determine the velocity (V) of the front and the periodicity of the pattern selected near the front (which is different from the equilibrium wavelength). Far enough in ahead of the front the equation of motion can be linearized around the homogeneous state (i.e., $\phi = \delta\phi + \langle \phi \rangle$) in a moving reference frame and solutions for velocity and periodicity can be obtained using the marginal stability condition as described in [22]. Briefly this calculation first determines the linear dispersion rate at the front, which is given by

$$\omega(k) = \frac{1}{2\tau} \left[\sqrt{1 + 4\tau\xi(k)} - 1 \right] + iVk, \quad (45)$$

with $\xi(k) = k^2 \left[\epsilon - (1 - k^2)^2 \right],$

where, $\delta\hat{\phi} \propto \exp[\omega(k)t]$, k is the wave-number and $\delta\hat{\phi}$ is the fourier transform of $\delta\phi$. A perturbation is marginally

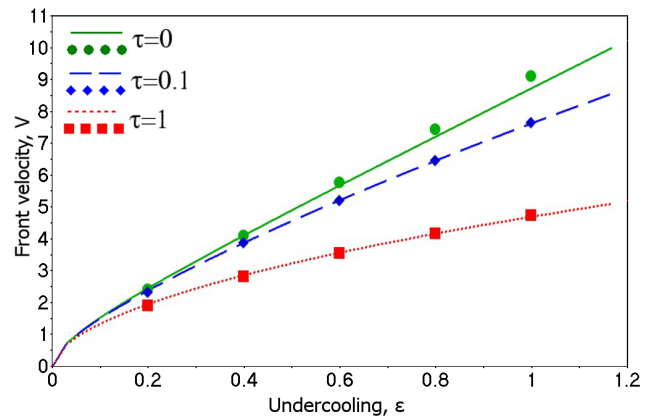


FIG. 6: (color on the web) Velocity V of the PFC-front *versus* undercooling ϵ as given by the results of present modeling (points) in comparison with the marginal stability predictions (curves), Eqs. (45)-(48).

stable at the moving front for $Re[\omega(k)] = 0$, i.e., the front neither grows nor decays exponentially at the amplification rate (45) as

$$V = \frac{1}{k_{im}^*} Re \left\{ \frac{1}{2\tau} \left[\sqrt{1 + 4\tau\xi(k^*)} - 1 \right] \right\}. \quad (46)$$

Here k^* is the selected wave-number assumed to be complex valued, $k^* = k_{re}^* + ik_{im}^*$ where k_{re}^* and k_{im}^* are the real and imaginary parts, respectively.

The most unstable mode at the front of the periodic stripes is given by the saddle-point $\partial\omega/\partial k = 0$ with $k = k^*$. Using the amplification rate (45), the saddle-point condition gives

$$iV + \frac{2k^* \left[\epsilon - 1 + 4(k^*)^2 - 3(k^*)^4 \right]}{\sqrt{1 + 4\tau\xi(k^*)}} = 0. \quad (47)$$

Finally, selection of the wave-number k_f at the front oscillating at angular frequency $Im[\omega(k^*)]$ is defined by

$$k_f = \frac{Im[\omega(k^*)]}{V}. \quad (48)$$

Using Eq. (45), the system of equations (46)-(48) was solved numerically [22] to predict the selection of the wave-number $k_f(\epsilon)$ and lattice parameter $a_f(\epsilon) = 2\pi/k_f(\epsilon)$ at the front moving with the velocity $V(\epsilon)$.

B. Algorithm for numerical results of the velocity and wave-number

The velocity and wave-number selected can be obtained by direct numerical simulation of the PFC-equation. After reaching stationary regime the determination of these quantities was obtained using the following algorithm,

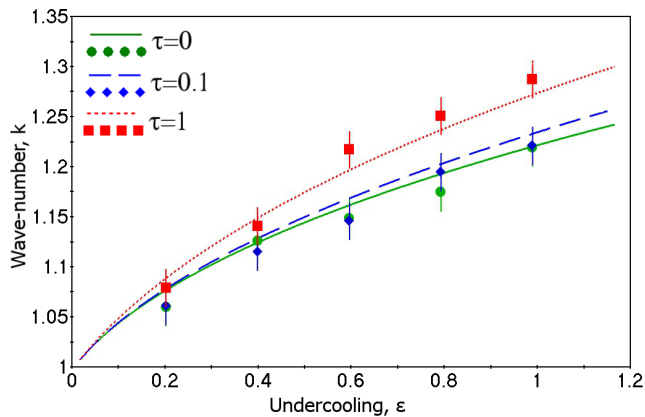


FIG. 7: (color on the web) Wave-number k_f selected at the PFC-front as a function of undercooling ε . The present modeling results (points) are compared with the predictions of marginal stability analysis (curves), Eqs. (45)-(48).

TABLE I: Modeling predictions for wave-numbers calculated for different grids and various averaged procedure

ε	mesh	$k(a_0)$	$k(a_1)$	$k(a_2)$	$k(a_{01})$	$k(a_{12})$	$k(a_{02})$	$k(a)$
0.1	regular	1.047	1.026	1.026	1.036	1.026	1.036	1.033
	adapted	1.023	1.016	1.010	1.020	1.013	1.016	1.016
0.4	regular	1.169	1.169	1.1424	1.169	1.1555	1.1555	1.16
	adapted	1.1284	1.1152	1.1010	1.1218	1.1080	1.1145	1.1148
0.6	regular	1.226	1.197	1.197	1.211	1.197	1.211	1.206
	adapted	1.195	1.180	1.161	1.187	1.170	1.178	1.178

1. Find the peak or maximum with a height above $\phi \geq \langle \phi \rangle + 0.1$ farthest the initial perturbation position. This peak will be denoted x_0 , the next farthest as x_1 , etc., as shown in Fig. 5. The distance between successive peaks can then be used to calculate the selected lattice parameter or wave-vector.
2. Compute the distances between neighboring peaks (see inset in Fig. 5). Then, the required lattice parameters a_i is

$$\begin{aligned}
 a_0 &= x_0 - x_1, & a_1 &= x_1 - x_2, & a_2 &= x_2 - x_3, \\
 a_{01} &= \frac{a_0 + a_1}{2}, & a_{12} &= \frac{a_1 + a_2}{2}.
 \end{aligned}
 \quad (49)$$

Calculate average lattice parameter by its mean value:

$$a = \frac{a_{01} + a_{12}}{2}. \quad (50)$$

3. After calculation of lattice parameter a , the wave-number k_f on the front is computed by $k_f = 2\pi/a$.
4. Calculate the front velocity as a displacement of initial point x_0 divided by time step: $V = [x_0(t + \Delta t) - x_0(t)]/\Delta t$.

Calculated values of the wave-number k_f are strongly dependent on the computational grid used in numerical simulations. With refinement grid, values of k_f converge

to the value necessary to obtain the prediction. As an example, Table I gives values for wave-numbers $k(a_i)$ calculated with different grids and from the values of the lattice parameter a_i given by Eqs. (49) and (50).

C. Comparison

For the numerical calculations the initial condition was such that $\phi_{x>0} = 0$ and $\phi_{x=0}$ has been set to be random numbers chosen between 0 and 0.01. The initial size of the system was 1000×10 , with a grid spacing of the initial regular mesh $h = 0.125$ and a minimal grid spacing in the adapted mesh as $h_{min} = 1 \cdot 10^{-4}$. This grid was used to obtain the results summarized in Table I. The size of this system is large enough that steady state profiles were obtained before the boundary conditions interfered.

Our computational domain has been chosen to be a quasi-one-dimensional region to provide comparison with the marginal stability analysis [22] in one-dimensional space. All comparisons for the wavelength selection have been made for the stripes. In the numerical simulations the stripes propagate in the direction perpendicular to their geometrical axes.

The marginal stability results are only valid far from the front in which the linearization is valid. For this reason the comparison should work the best farthest from the front. The inset in Fig. 5 gives an example of the peak positions chosen for the study. Comparison of the numerically calculated front velocity and wave-number (dots in plots) with predictions of the marginal stability described by Eqs. (45)-(48) (lines in plots) are summarized in Figs. 6 and 7, respectively. It can be seen from Fig. 6 that the velocity V obtained in the present modeling for stripes propagation is perfectly consistent with the front velocity described by the criterion of marginal stability. The wave-number k calculated on the front of modeled stripes is also consistent with k_f selected on the front of periodic pattern analytically predicted by the marginal stability criterion (Fig. 7). Although calculated wave-numbers (see rounds, diamonds and squares in Fig. 7) exhibit some deviations from the curves given by the marginal stability criterion, they depend on their averaged values obtained for different computational grids (see Table I) and from wavelengths for different peaks in periodic pattern on the front (see inset in Fig. 5). As a result, the wave-numbers obtained in the present modeling have error bars which include the curves given by the criterion of marginal stability (see Fig. 7). Hence, the present numerical algorithm and its numerical realization exhibit quantitative agreement with the results obtained from the marginal stability analysis described by Eqs. (45)-(48).

VIII. CONCLUSIONS

An unconditionally stable time integration algorithm for the solution of the hyperbolic phase-field crystal model equation is presented. Variational formulation of the model has allowed us to use a finite-element method for numerical simulation using standard C^0 -continuous Lagrange elements (available in modern program packages). As a result, a second order accurate finite-element numerical scheme has been developed, which is unconditionally stable and ensures that free energy decreases as patterns evolve and become constant in the steady state.

The numerical scheme was shown to give results consistent with the phase diagram of the model constructed from a one mode approximation in the appropriate limit. Additionally the scheme was shown to be quantitatively consistent with the predictions of marginal stability theory for velocity and wave-vector selection of a striped phase invading an unstable homogeneous state. These results confirm the applicability of the present algorithm

and numerical scheme to theoretically important and practically significant quantitative predictions.

Acknowledgments

P. K. G. acknowledges the partial support within the framework of the program 07.08 “Research Investigations in Education”, project No. 2.947.2011. He also grateful for support from the Administration of the Physical Faculty during his stay in Oakland University (Rochester, MI). H. G. acknowledges support from Xunta de Galicia and the European Research Council through the FP7 Ideas Starting Grant program (project No. 307201). N. V. K. thanks support from German Foundation of Scientific Exchanges, Stipendium A/11/94255 (DAAD - Deutscher Akademischer Austausch Dienst). K. R. E. acknowledges support from NSF under Grant No. DMR-0906676.

-
- [1] K. R. Elder, M. Katakowski, M. Haataja, and M. Grant, Phys. Rev. Lett. **88**, 245701 (2002).
- [2] K. R. Elder and M. Grant, Phys. Rev. E **70**, 051605 (2004).
- [3] K. R. Elder, G. Rossi, P. Kanerva, F. Sanches, S.-C. Ying, E. Granato, C. V. Achim, and T. Ala-Nissila, Phys. Rev. Lett. **108**, 226102 (2012).
- [4] K. R. Elder, N. Provatas, J. Berry, P. Stefanovich, and M. Grant, Phys. Rev. B **75**, 064107 (2007).
- [5] T. V. Ramakrishnan and Y. Yussouff, Phys. Rev. B **19**, 2775 (1979); R. Evans, Adv. Phys. **28**, 143 (1979); Y. Singh, Phys. Rep. **207**, 351 (1991).
- [6] Y. M. Jin and A. G. Khachaturyan, J. Appl. Phys. **100**, 013519 (2006).
- [7] H. Emmerich, H. Löwen, R. Wittkowski, T. Gruhn, G. I. Toth, G. Tegze, and L. Granasy, Advances in Physics **61**, 665 (2012).
- [8] P. Stefanovic, M. Haataja, and N. Provatas, Phys. Rev. Lett. **96**, 225504 (2006); Phys. Rev. E **80**, 046107 (2009).
- [9] P. Galenko, D. Danilov, and V. Lebedev, Phys. Rev. E **79**, 051110 (2009).
- [10] J. A. Ramos, E. Granato, S. C. Ying, C. V. Achim, K. R. Elder, and T. Ala-Nissila, Phys. Rev. E **81**, 011121 (2010).
- [11] S. M. Wise, C. Wang, and J. S. Lowengrub, SIAM J. Numer. Anal. **47**, 2269 (2008).
- [12] V. Lebedev, A. Sysoeva, and P. Galenko, Phys. Rev. E, **83**, 026705-1-11 (2011).
- [13] C. Wang and S. M. Wise, SIAM J. Numer. Anal. **49**, 945 (2011).
- [14] A. Baskaran, J. S. Lowengrub, C. Wang, and S. M. Wise, *Convergence analysis of a second-order convex splitting scheme for the modified phase field crystal equation*, SIAM J. Numer. Anal. (2013) *under review*.
- [15] D. J. Eyre, An unconditionally stable one-step scheme for gradient systems, unpublished, www.math.utah.edu/~eyre/research/methods/stable.ps
- [16] D. J. Eyre, in *Computational and Mathematical Models of Microstructural Evolution*, MRS Proceedings Volume 529, edited by J. W. Bullard, L. Q. Chen, R. K. Kalia, and A. M. Stoneham (The Materials Research Society, Warrendale, PA, 1998), pp. 3946.
- [17] B. P. Vollmayer-Lee and A. D. Rutenberg, Phys. Rev. E. **68**, 66703 (2003).
- [18] M. Cheng and J. A. Warren, Phys. Rev. E **75**, 017702 (2007); M. Cheng and J. A. Warren, J. Comp. Phys. **227**, 6241 (2008).
- [19] H. Gomez and T. J. R. Hughes, J. Comp. Phys. **230**, 5310 (2011).
- [20] H. Gomez and X. Nogueira, Comput. Methods Appl. Mech. Engrg. **249-252**, 52 (2012).
- [21] H. Gomez, V. M. Calo, Y. Bazilevs, and T. J. R. Hughes, Comput. Methods Appl. Mech. Engrg. **197**, 4333, (2008).
- [22] P. K. Galenko and K. R. Elder, Phys. Rev. B, **83**, 064113-1-8 (2011).
- [23] R. Backofen, A. Rätz, and A. Voigt, Philosophical Magazine Letters, **87**(11) (2007) 813-820.
- [24] O. K. Zienkiewicz, *The Method of Finite Elements in Engineering*, (McGraw-Hill, New York, 1977); L. J. Segerlind, *Applied Finite Element Analysis*, 2nd Edition (Wiley, New York, 1984).
- [25] <http://www.freefem.org>
- [26] F. Hecht, The mesh adapting software: bamg. INRIA report 1998 (<http://www-rocq.inria.fr/gamma/cdrom/www/bamg/eng.htm>); B. Mohammadi and F. Hecht, Revue Européene des Éléments Finis **10**(5), 575 (2001).
- [27] P. Galenko and D. Jou, Phys. Rev. E **71**, 046125 (2005); P. Galenko and D. Jou, Physica A **388**, 3113 (2009).
- [28] G. Dee and J. S. Langer, Phys. Rev. Lett. **50**, 383 (1983); E. Ben-Jacob, H. Brand, G. Dee, L. Kramer, and J. S. Langer, Physica **14D**, 348 (1985); W. van Saarloos, Phys. Rep. **386**, 29 (2003); R. Goh, S. Mesuro, and A. Scheel, SIAM J. Appl. Dyn. Sys. **10**, 360 (2011).

- [29] M. Zukerman, R. Kupferman, O. Shochet, and E. Ben-Jacob, *Physica* **90D**, 293 (1996).